Microchemical Journal 205 (2024) 111244

Contents lists available at ScienceDirect

Microchemical Journal

journal homepage: www.elsevier.com/locate/microc

Potential-dependent simultaneous detection of uric acid and glucose using dual-function Ni@CNT supported carbon fiber electrodes

Biyuan Zhou [a], Jijiang Fu [a], Yonghao Yuan [a], Fang Han [b,*], Kaifu Huo [c], Paul K. Chu [d], Xuming Zhang [a,*]

[a] The State Key Laboratory of Refractories and Metallurgy and Institute of Advanced Materials and Nanotechnology, Wuhan University of Science and Technology, Wuhan 430081, China
[b] School of Chemistry and Chemical Engineering, Wuhan University of Science and Technology, Wuhan 430081, China
[c] Wuhan National Laboratory for Optoelectronics (WNLO), School of Optical and Electronic Information, Huazhong University of Science and Technology, Wuhan 430074, China
[d] Department of Physics, Department of Materials Science and Engineering, and Department of Biomedical Engineering, City University of Hong Kong, Tat Chee Avenue, Kowloon, Hong Kong, China

ARTICLE INFO

Keywords:
Ni nanoparticles embedded CNT
Uric acid
Glucose
Potential-dependent sensing
Dual-function sensor

ABSTRACT

The development of non-enzyme electrochemical sensors is crucial for rapid and convenient detect the biomarkers of diabetes mellitus and hyperuricemia. In this study, we developed a bifunctional electrode comprising a core–shell Ni@CNT anchored on carbon fibers (CFs) and proposed potential-dependent techniques for simultaneous detection of UA and glucose. By adjusting the pH value of electrolyte to balance the oxidation potentials and signal intensities of UA and glucose, the Ni@CNT-CF electrode demonstrated good selectivity and wide linear range from 1 μM to 1 mM for UA at 0.2 V and 1 μM to 6 mM for glucose at 0.6 V. It also exhibited high sensitivity of 1.86 μA mM^{-1} μg^{-1} for UA and 1.52 μA mM^{-1} μg^{-1} for glucose, with low detection limits of 0.32 and 0.39 μM, respectively. These excellent performance attributes to the high conductivity and corrosion resistance of CNT and high catalytic activity of embedded Ni nanoparticles. Furthermore, the Ni@CNT-CF electrode demonstrated significant recoveries of UA and glucose in both simulated fluid and real blood samples, highlighting its potential for practical applications in UA and glucose detection.

1. Introduction

With the improvement of living standards, significant changes in dietary habits have led to a notable increase in the incidence of gout, kidney disease, cardiovascular disease, and diabetes mellitus [1–5]. Early detection of specific biomarkers such as uric acid (UA) and glucose in body fluids is crucial for preventing and managing these conditions. Recent studies have shown that prolonged hyperuricemia can interfere with glucose metabolism, potentially induce diabetes [6]. Therefore, there is an urgent need to develop efficient and economical sensors capable of simultaneously and facilely detecting glucose and UA.

Current detection methods include colorimetric enzyme assays [7–11], liquid chromatography analysis [12–15], surface enhanced Raman scattering [16–20], and electrochemical techniques [21–30]. Among these, electrochemical methods stand out for their simplicity, rapid response, high sensitivity, and cost-effectiveness. Transition metals and metal oxides, such as Co_3O_4, CuO, ZnO, NiO, and Ni, have been widely employed for enzyme-free electrochemical glucose sensing due to the strong oxidizing ability of the electrocatalytic MOOH layer in high-pH environments [31–33]. Carbon-based nanocomposites are commonly used for UA detection [34–36]. To ensure simultaneous detection the UA and glucose, transition metal or oxide nanoparticles are always decorated on the surface of carbon nanotubes (CNTs) [37,38]. For example, Wang et al. introduced a flexible sensor comprising copper microspheres modified ZnO@CNT, enabling simultaneous sensing of UA and glucose with rapid response times and high sensitivity [39]. Similarly, Li et al. developed a copper and cerium bimetallic nanoparticles-modified graphene and single-walled CNTs electrode, demonstrating positive correlation with dopamine (DA) and UA, and negative correlation with glucose [40]. However, these complex surface modifications often sacrifice the surface activity of CNTs and electron transport efficiency of the electrode, resulting in poor

* Corresponding authors.
E-mail addresses: huang873@126.com (F. Han), xumzhang@wust.edu.cn (X. Zhang).

https://doi.org/10.1016/j.microc.2024.111244
Received 22 May 2024; Received in revised form 29 June 2024; Accepted 17 July 2024
Available online 18 July 2024

sensitivity, selectivity, and a narrow linear detection range. Additionally, the adjacent oxidation potentials of UA and glucose cause the electrical signals to interfere with each other. Notably, the metal Ni electrode responded to glucose only in alkaline media, the carbon-based electrode responds well to UA and is optimal in neutral media (Fig. S1). This inspired us to rationally design electrode structures comprising both metal and CNTs, along with an appropriate electrolyte system, to effectively and selectively detecting both UA and glucose simultaneously.

Herein, we developed core–shell Ni@CNT nanostructure anchored on carbon fibers (CFs) electrodes using a facile CVD method with nickel nanoparticles as catalyst for CNT growth. The integration of Ni nanoparticles within CNTs enhances sensor performance by providing several advantages. Firstly, the embedded nickel nanoparticles act as highly active centers for glucose sensing while being protected against electrolyte corrosion by carbon shells. Secondly, the large surface area of CNTs facilitates efficient adsorption and oxidation of UA molecules, enhancing sensitivity. Thirdly, the high electrical conductivity of carbon nanotubes and carbon fibers ensures the efficient transfer of electrons from the active site to the current collector, while direct growth on carbon fibers provides excellent structural stability for long-term high performance. By adjusting the pH of the electrolyte, we balanced the oxidation potentials and signal intensities of UA and glucose. The Ni@CNT-CF electrode demonstrated excellent performance, with UA detection at 0.2 V showing a linear response from 1 μM to 1 mM, a sensitivity of 1.86 μA mM^{-1} μg^{-1}, and a detection limit of 0.32 μM. For glucose detection at 0.6 V, a linear range from 1 μM to 6 mM was achieved, with sensitivities of 1.52 μA mM^{-1} μg^{-1} and a detection limit of 0.39 μM. Both UA and glucose sensing exhibited fast response times of 3.7 s and 2.8 s, respectively. Test results from simulated liquid and blood samples were consistent with commercially available meters, showing that Ni@CNT-CF electrodes have good potential for simultaneous UA and glucose sensing in practical use.

2. Experimental

2.1. Materials

Polyacrylonitrile (PAN, Mw = 150,000), N, N-dimethylformamide (DMF, C_3H_7NO), nickel(II) acetate tetrahydrate ($Ni(CH_3COO)_2{\cdot}4H_2O$), acetone ($C_3H_6O$), glucose (Glu), Uric Acid (UA), ascorbic acid (AA), dopamine (DA), sodium sulfate (Na_2SO_4), potassium chloride (KCl), sodium chloride (NaCl), magnesium sulfate ($MgSO_4$), and potassium hydroxide (KOH) were purchased from National Pharmaceutical. Phosphate-buffered saline (PBS) solutions were prepared using a Mettler Toledo pH meter. Deionized water with a resistivity exceeding 18 MΩ cm, obtained from a Millipore-Q water purification system, was used in all experiments.

2.2. Characterization

The crystal structure, morphology and chemical composition of the samples were analyzed using field emission scanning electron microscopy (FE-SEM, Apreo S HiVac, Germany), transmission electron microscopy (TEM, FEI Tecnai G2 F20, USA), and energy dispersive X-ray spectroscopy (EDS, XPLORE, UK). Phase analysis was conducted using an X-ray diffractometer (XRD, Smart lab, Japan).

2.3. Preparation of CF by electrostatic spinning

Polyacrylonitrile (PAN) fibers were conducted using electrostatic spinning technology. Typically, 1.2 g of PAN powder was dissolved in 10 mL of N, N-dimethylformamide (DMF) and stirred magnetically at 60 °C for 12 h to prepare the spinning solution. The solution was then electrospun onto aluminum foil at 15–17 kV and dried at 60 °C for 24 h to obtain organic fibers. The PAN fibers were subsequently stabilized in air at a heating rate of 5 °C min^{-1} to 280 °C for 1 h. Following stabilization, the samples were carbonized to prepare carbon fibers (CFs) in an argon (Ar) atmosphere at 800 °C for 2 h.

2.4. Synthetic Ni@CNT-CF

To synthesize Ni@CNT-CF, carbon fibers (CFs) were initially immersed in an ethanol solution containing 0.01 M nickel acetate for 10 min. Subsequently, the treated CFs were removed and air-dried, resulting in nickel acetate-coated CFs. The nickel acetate-coated CFs were then placed in a tube furnace with an Ar/H_2 flow rate of 100 sccm. The furnace was heated to 850 °C at a rate of 10 °C min^{-1} and maintained at this temperature for 1 h. During the stabilization period, the Ar/H_2 gas was turned off, and acetone was introduced into the reaction chamber with Ar at a flow rate of 100 sccm. After the reaction, the chamber was purged with pure Ar until the temperature reached room temperature. Finally, the Ni@CNT-CF product was collected for further characterization.

2.5. Electrochemical measurement

A three-electrode system was employed with a Pt filament (φ0.5 × 37 mm) and saturated calomel electrode (SCE) as the counter electrode and reference electrode, connected to CHI 760e electrochemical workstation (CH Instruments, Chenhua Corp, China). The work electrode was prepared by dropping 5 μL of Ni@CNT-CF suspension (50 μg, 10.0 mg mL^{-1}) on the clean glassy carbon electrode (GCE) surface and dried at room temperature. Electrochemical tests were conducted using cyclic voltammetry (CV), constant potential tests, and multi-potential step tests.

For the simulation study, a mixed solution containing of 400 μM UA and 5 mM glucose was prepared. In a multi-potential step test, 1 mL of the simulated fluid is added three times in succession to 4 mL of 0.1 M KOH solution for measurement. The amperometric response of the Ni@CNT-CF electrode towards real samples (serum obtained by centrifugation and filtration of human blood) was evaluated by adding 500 μL serum to 5 mL 0.1 M KOH solution and process at 0.2 V and 0.6 V. Recovery was calculated according to the following equation:

$$C_1 = \frac{\left(\frac{\Delta I}{K}\right) \times V_t}{V_s} \quad (1)$$

$$\text{Recovery} = \frac{C_1}{C} \times 100\% \quad (2)$$

C_1 stand for measured concentration by electrochemical method. Where the ΔI stand for current increment after adding simulated fluid or serum measured at 0.2 V and 0.6 V, the K is the sensitivity towards UA and glucose, the V_t stand for the total volume of matrix solution, the V_s stand for the volume of added simulated fluid. C is the standard values for the concentration of glucose and UA in simulated fluid and serum. For serum, the values are measured in hospital using colorimetric enzyme assays. For comparison, the content of UA and glucose in simulated fluid and serum was also measured using a commercial enzyme-based uric acid and glucose meter (Sinocare, EA-19).

3. Result and discussion

3.1. Synthesis and characterization of Ni@CNT-CF

Fig. 1 illustrates the synthesis process of Ni@CNT-CF. Initially, an organic fiber was fabricated using the electrostatic spinning technique, followed by heat treatment to obtain the CFs [41,42]. Scanning electron microscopy (SEM) analysis revealed a smooth surface of the CFs with diameters ranging from 200 to 300 nm (Fig. 2a). CNTs are then formed

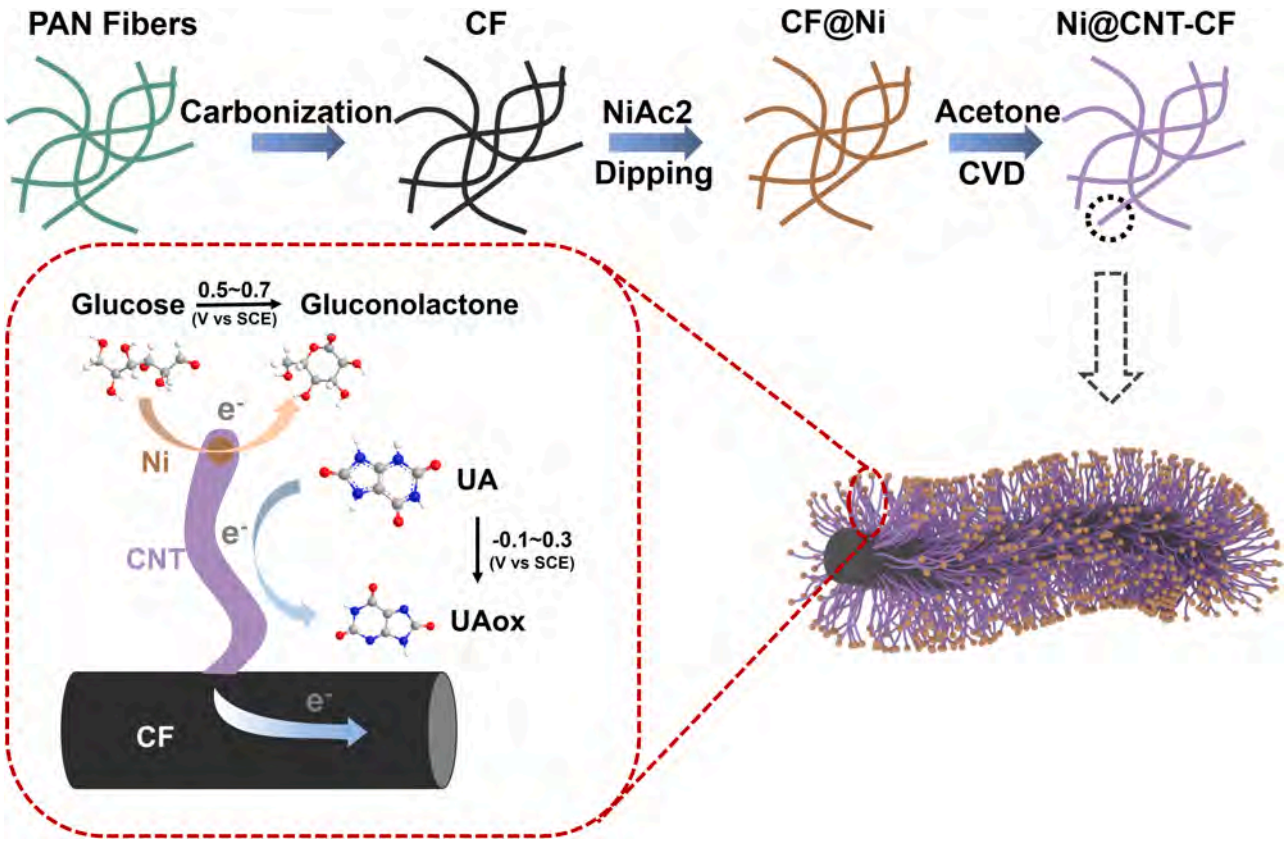

Fig. 1. The schematic diagram of synthesizing the Ni@CNT-CF.

on the CF by loading Ni onto the CF surface through a simple soaking process followed by chemical vapor deposition (CVD) treatment [43,44]. Fig. 2b and c display the morphology of Ni@CNT-CF, showcasing high-density CNTs uniformly grown on the fibers. The CNTs are hundreds of nanometers in length and less than 50 nm in diameter. Transmission electron microscopy (TEM) images in Fig. 2d–e illustrate the tight integration of CNTs grown on CFs, with well-crystallized carbon layers wrapping around nanoparticles approximately 5 nm in size. High-resolution TEM revealed a lattice spacing of 0.20 nm for the nanoparticle, corresponding to the (1 1 1) crystal plane of metal nickel (Fig. 2f). Energy-dispersive X-ray spectroscopy (EDS) spectra in Fig. 2g–i confirmed a large amount of uniformly distributed carbon and a small amount of nickel in Ni@CNT-CF. These results collectively validate the successful fabrication of the core–shell Ni@CNT structure on CF.

Fig. 3a presents the X-ray diffraction (XRD) pattern of Ni@CNT-CF. The observed peaks at 44.5°, 51.8°, and 76.3° correspond to the (1 1 1), (2 0 0), and (2 2 0) crystal planes of metal nickel (JCPDS: 04-0850), along with graphitic carbon at 25.3° (JCPDS: 41-1487). No distinct peaks attributable to nickel salt were observed after immersion. Fig. 3b displays the full X-ray photoelectron spectroscopy (XPS) spectrum of Ni@CNT-CF, highlighting the presence of carbon and oxygen elements. The high-resolution Ni 2p in Fig. 3c shows two weak peaks fitted at 857.2 eV and 853.3 eV, corresponding to Ni^{2+} in oxide and metal Ni, respectively [45,46]. Fig. 3d presents the C 1 s spectrum, revealing four fitted peaks at 284.6 eV and 285.7 eV for sp^2 and sp^3 carbon, and at 287 eV and 289.5 eV for C-O and C=O bonds [47,48]. The Raman spectrum of Ni@CNT-CNF is shown in Fig. S2. There is no vibration mode in the range of 400 ~ 1000 cm^{-1}, indicating that there is no residual nickel oxide left on the surface of CFs [49]. Two characteristic bands corresponding to the D and G bands of graphitic carbon were observed at 1350 cm^{-1} and 1570 cm^{-1}, respectively. The I_D/I_G value, which reflects the defect density of carbon-based materials [50], was found to be 1.21 for Ni@CNT-CF, higher than that of commercial CNTs (I_D/I_G=1.08). This indicates a higher concentration of defects in Ni@CNT-CF, which may enhance the adsorption and catalytic activity of CNT to UA molecules.

3.2. Electrochemical tests

The cyclic voltammetry (CV) curves of the Ni@CNT-CF electrode in 0.1 M KOH under varying scanning rates are shown in Fig. 4a. A linear relationship between the peak currents and the square root of the scanning rate (R>0.99) indicates a diffusion-controlled electrochemical process on the Ni@CNT-CF electrode surface, facilitating the detection of reactive substances. The electrochemical response of the Ni@CNT-CF electrode towards glucose and UA was further explored under different KOH concentrations. Reversible redox peaks associated with the $NiOOH/Ni(OH)_2$ redox couple were observed between 0.3 V and 0.7 V (vs. SCE) for KOH concentrations ranging from 0.01 M to 1 M (Fig. S3). A significant shift in peak potential and a drop in oxidation peak current were observed at 0.01 M KOH, indicating that the redox reaction on the Ni nanoparticles surface is influenced by OH^- concentration. It is well known that the NiOOH is the key intermediate for glucose oxidation, which is then reduces to $Ni(OH)_2$. The subsequent electrochemical oxidation of $Ni(OH)_2$ to NiOOH further increases the oxidation current peak [45], establishing a proportional relationship between the electrical signal and glucose concentration within a specific range. Similar linear relationships between the oxidation peak current and glucose concentration were observed in both 0.1 M and 1 M KOH electrolytes, while low slop linear behavior was observed at 0.01 M KOH (Fig. 4b and Fig. S4). Without the Ni species, bare CNTs showed no response to glucose but were sensitive to UA in alkaline solutions (Fig. S5). The CV curves of the Ni@CNT-CF electrode towards UA in different KOH concentrations revealed no linear behavior in the potential range from 0.3 V to 0.7 V, suggesting that the redox couple is not the active site for UA sensing. However, at low potential ranging from −0.2 to 0.3 V, a linear

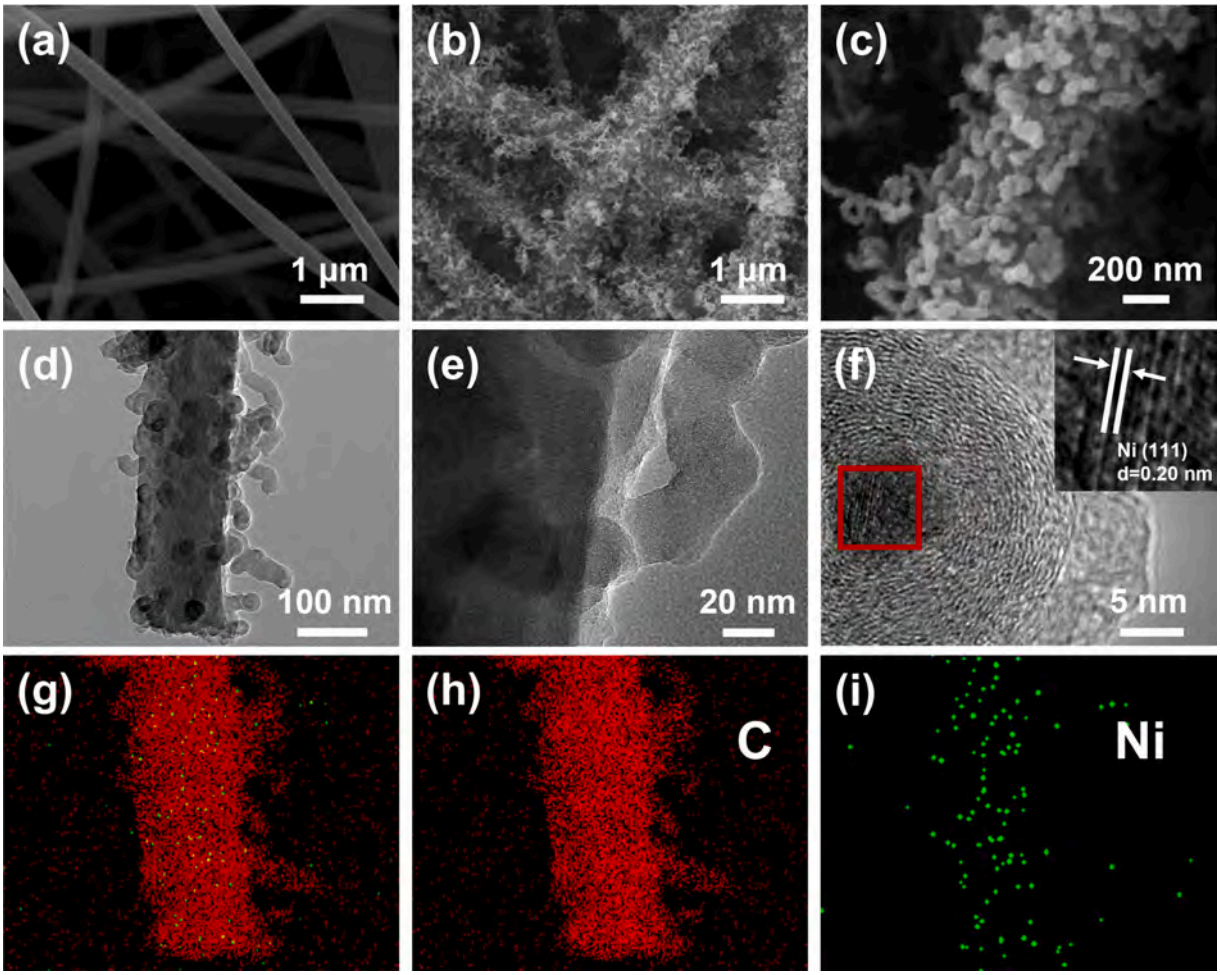

Fig. 2. (a) SEM of bare CF; (b, c) SEM of Ni@CNT-CF; (d, e, f) TEM of Ni@CNT-CF and (g, h, i) Elemental mappings of Ni@CNT-CF.

relationship between the enhanced anodic peak current and concentration of UA are observed. At high concentration of KOH, the peak potential negatively shifts and peak current decreases (Fig. 4c and Fig. S6). According to above results, it is confirmed that the active center towards glucose and UA are relays on Ni and CNT, respectively, and their potential difference is increases with the decrease of KOH concentration, as elucidated by the Nernst equation (Table S1), suggesting a possible way to reduce signal interference between glucose and UA by reasonably choosing the media pH, herein, the optimal conditions for simultaneous glucose and UA sensing were identified using 0.1 M KOH media. Fig. 4d displays the CV curves of the Ni@CNT-CF electrode in 0.1 M KOH solution with glucose and both glucose and UA. Upon addition of 1 mM glucose, a current enhancement is observed between 0.4 and 0.6 V, with no response observed between −0.2 and 0.3 V. In an alkaline solution containing both 4 mM glucose and 400 μM UA, an increased current is clearly observed between −0.2 and 0.3 V, accompanied by negligible peak current fluctuations between 0.4 and 0.6 V. These findings further validate the Ni@CNT-CF electrode's capability for simultaneous detection of UA and glucose across distinct potential ranges.

To identify the optimal potential for the Ni@CNT-CF electrode in sensing UA and glucose, constant potential tests were conducted in 0.1 M KOH. Amperometric responses were recorded by sequentially adding 200 μM glucose at potentials ranging from 0.5 V to 0.7 V (Fig. S7). The results indicated an increasing linear slope with rising voltage, stabilizing between 0.6 V and 0.7 V. However, higher potentials resulted in increased background currents due to water electrolysis. Fig. 5a illustrates the glucose current response ranging from 1 μM to 6 mM at 0.6 V. The corresponding calibration curve in Fig. 5b revealed two linear ranges from 1 to 100 μM with a sensitivity of 1.52 μA mM^{-1} μg^{-1} (correction coefficient R=0.998) and 100 to 6000 μM with a sensitivity of 0.3 μA mM^{-1} μg^{-1} (correction coefficient R=0.991). The lack-of-fit test also indicates the high confidence of this linear range (Table S2). The detection limit was calculated to be 0.39 μM at a signal-to-noise ratio of 3, with a rapid response time reaching a steady state within 2.8 s, comparable with or outperforming most non-enzymatic glucose sensors (Table S3) [11,39,40,51–54]. The optimal potential range for UA detection was determined by sequentially adding 20 μM UA at potentials ranging from −0.1 V to 0.3 V in 0.1 M KOH (Fig. S8). The linear slope increased with higher potentials, but interference from glucose oxidation was observed at 0.3 V. Therefore, 0.2 V was selected as the optimal potential for UA detection to minimize signal interference. Fig. 5d presents the amperometric response to sequentially added UA concentrations at 0.2 V. The resulting calibration curve displayed two linear ranges from 1 to 20 μM with sensitivity of 1.86 μA mM^{-1} μg^{-1} and 20 to 1000 μM with sensitivity of 0.42 μA mM^{-1} μg^{-1}. The detection limit was determined to be 0.32 μM at a signal-to-noise ratio of 3, with a rapid current response within 3.7 s (Fig. 5e).

Anti-interference capability is crucial for sensor applications. To evaluate the mutual interference between glucose and UA using the Ni@CNT-CF electrode, amperometric responses were recorded by continuously adding 5 mM glucose and 200 μM UA at 0.2 V and 0.6 V in 0.1 M KOH, respectively (Fig. 5c and f). At 0.6 V, 200 μM UA interference added to 5 mM glucose media resulted in a negligible current response of 3.4 %. Similarly, at 0.2 V, there was no obvious current response by adding 5 mM glucose in uric acid medium, further

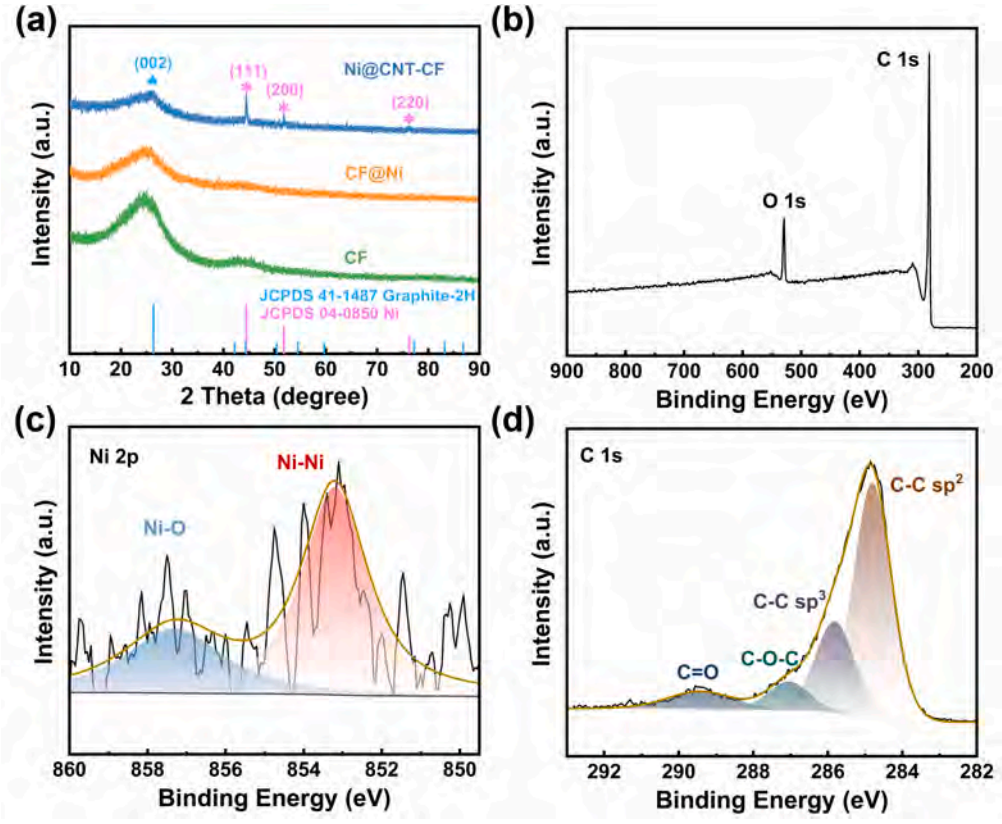

Fig. 3. (a) XRD patterns of CF, CF@Ni, and Ni@CNT-CF; (b) XPS full spectra of Ni@CNT-CF; (c) Ni 2p; (d) C 1 s.

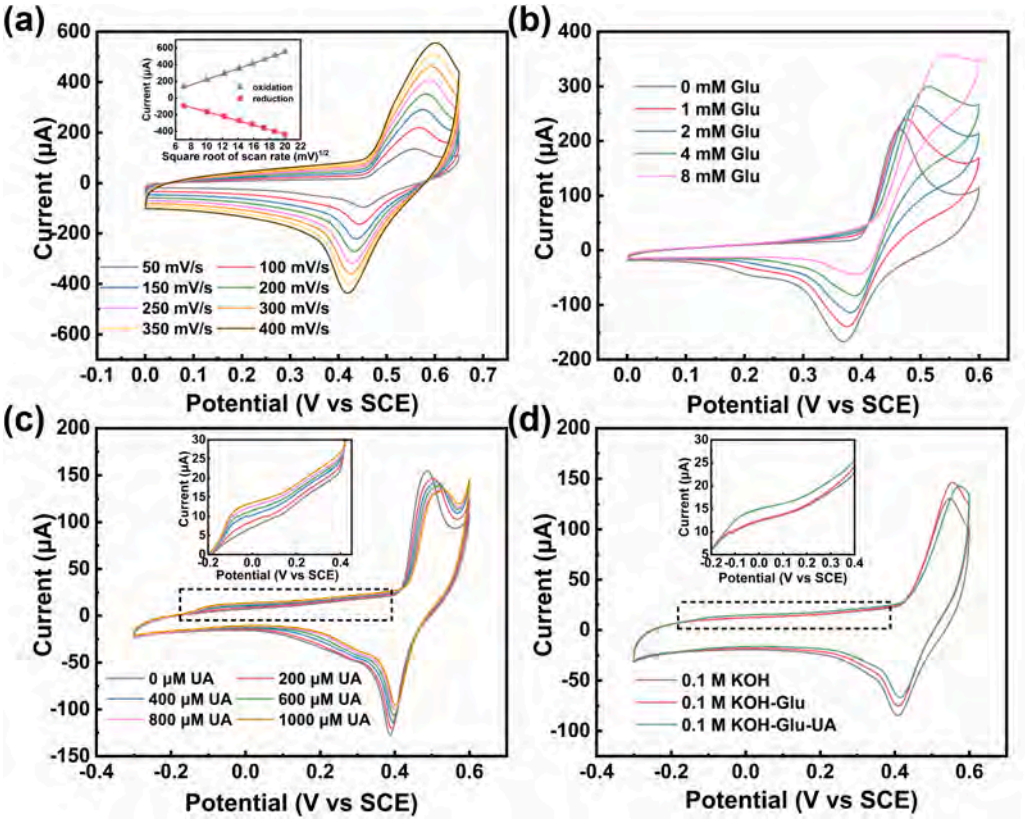

Fig. 4. (a) CV curves at different sweep rate in 0.1 M KOH solution, inserted picture is the linear relationships between peak oxidation and reduction currents fitted to the square root of the sweep rate; (b) CV curves at different amounts of glucose in 0.1 M KOH at a sweep rate of 100 mV/s; (c) CV curves at different UA concentrations in 0.1 M KOH solution at a sweep rate of 100 mV/s; (d) CV curves of UA and glucose coexisting in 0.1 M KOH at a sweep rate of 100 mV/s.

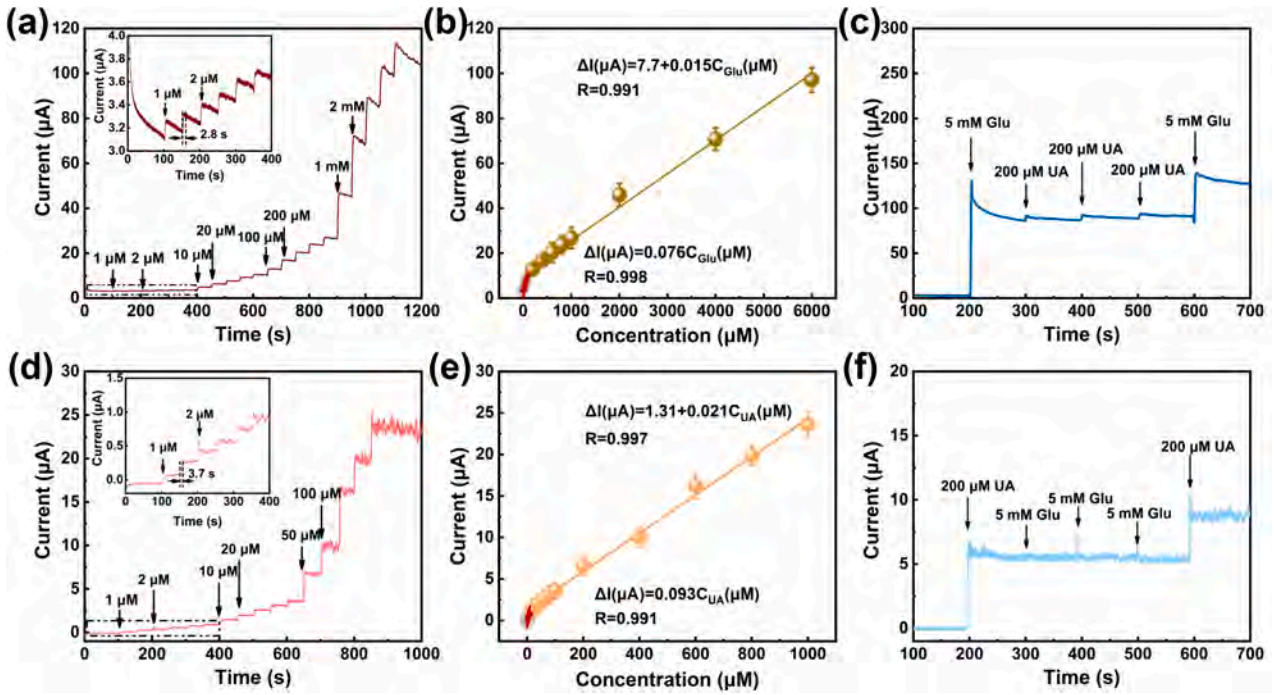

Fig. 5. (a) I-t curve of Ni@CNT-CF after continuous injection different amounts of glucose at 0.6 V in 0.1 M KOH; (b) The fits line for glucose determination with two liner ranges; (c) Interference testing between UA and glucose detection at 0.6 V; (d) I-t curve of Ni@CNT-CF after continuous adding different amounts UA at 0.2 V in 0.1 M KOH; (e) The fits line for UA determination with two liner ranges; (f) Interference testing between UA and glucose detection at 0.2 V.

confirming the good electivity between the glucose and UA by potential selection. To assess potential interference from other organic and inorganic compounds commonly found in blood, interference tests were performed by adding 50 μM AA, 10 μM DA, 1 mM potassium chloride, 1 mM sodium chloride, and 1 mM magnesium sulfate to 0.1 M KOH containing 200 μM UA or 5 mM glucose (Fig. S9). At 0.6 V, these interferents exhibited negligible impact during glucose detection. At 0.2 V, small instantaneous current increment was observed when AA or DA was introduced to the UA-containing media, but gradually return to baseline. These results demonstrate that the Ni@CNT-CF electrode exhibits robust anti-interference capabilities between glucose and UA, as well as interference from other organic and inorganic compounds when appropriate potentials are selected.

The reproducibility and long-term stability of the Ni@CNT-CF electrode were assessed by measuring the anodic currents of cyclic voltammetry (CV) curves at 0.2 V and 0.6 V at a scanning rate of 100 mV/s in 0.1 M KOH for two weeks (Fig. S10). During the initial 5 days, the current strength for UA stabilized at 97 % and that of glucose stabilized at 93 %. After 14 days, these values remained above 95 % and 90 %, respectively, indicating excellent stability. Under the condition of 0.1 M KOH for 3000 cycles, the CV curves shows good reproducibility, further confirming the outstanding structure stability of the Ni@CNT-CF electrode (Fig. S11).

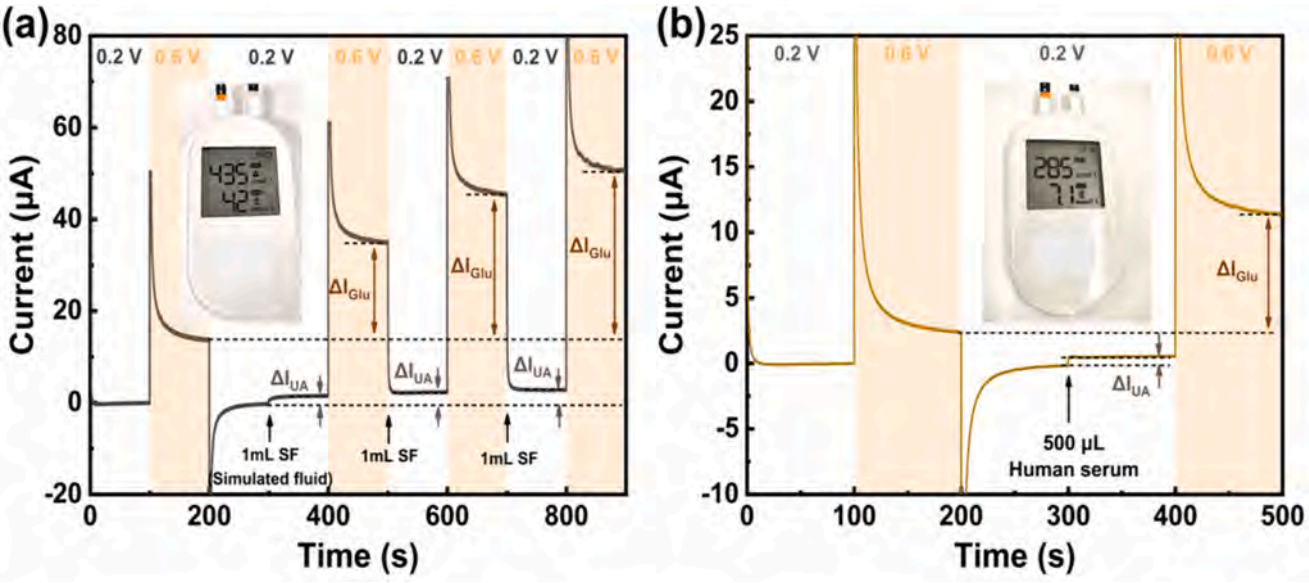

Fig. 6. I-t response to UA and glucose measurements at 0.2 V and 0.6 V on Ni@CNT-CF electrode with the addition of (a) simulated fluid and (b) serum samples.

3.3. Testing of simulated fluids and blood

Reliability is a crucial parameter for assessing the practical applicability of electrode materials. To evaluate the Ni@CNT-CF electrode's reliability, simultaneous detection of UA and glucose was performed in 0.1 M KOH using both simulated fluid and real serum samples. For the simulated solution containing 400 μM UA and 5 mM glucose, the current responses to UA and glucose were measured at 0.2 V and 0.6 V, respectively (Fig. 6a). Based on these current responses by successively adding 1 mL simulated fluid, the concentrations of UA and glucose detected by the Ni@CNT-CF electrode were calculated. The average recoveries of UA and glucose by electrochemical tests were 98.2 ± 5.7 % and 108.9 ± 4.7 %, respectively, which were better than the 108.7 % and 84 % obtained from the commercial meter. For the real serum samples, as shown Fig. 6b, the recoveries of UA and glucose by electrochemical testing based on the Ni@CNT-CF electrode were calculated to be 104.7 % and 104.5 %, respectively, which were better than the 109.6 % and 107.3 % obtained by commercial enzyme-based UA and glucose meter (Table S4). These results highlight the promising applicability of the Ni@CNT-CF electrode for the determination of UA and glucose concentrations in real serum samples, further affirming its reliability.

4. Conclusion

In summary, we developed a highly sensitive and highly selective enzyme-free electrochemical biosensor for glucose and UA detection, using core–shell Ni@CNT on a carbon fiber substrate prepared by simple immersion and chemical vapor deposition. Optimization of the electrolyte pH enhanced the synergy between the CNT and Ni particles, facilitating optimal bi-functional detection of UA and glucose at different potentials. The resulting Ni@CNT-CF electrode exhibited a broad linear range, rapid response time, low detection limit, high sensitivity, and selectivity. These attributes stem from the high catalytic activity, high conductivity and corrosion resistance of CNT for UA sensing and embedded metal Ni for glucose sensing. Specifically, the sensor achieved high sensitivities of 1.86 and 1.52 μA mM^{-1} μg^{-1}, wide detection ranges of 1 μM to 1 mM and 1 μM to 6 mM, and low detection limit of 0.32 and 0.39 μM for UA and glucose detection, respectively. Furthermore, the recoveries of UA and glucose in both simulated fluid is calculated to be 98.2 ± 5.7 %, 108.9 ± 4.7 % and in real blood specimens is 104.7 % and 104.5 %, respectively, indicating robust practicability. The exceptional sensing properties of the Ni@CNT-CF electrode pave the way for the development of non-enzymatic diagnostic devices capable of simultaneously detecting UA and glucose, offering promising prospects for practical use.

CRediT authorship contribution statement

Biyuan Zhou: Writing – original draft, Formal analysis, Data curation. **Jijiang Fu:** Writing – original draft, Formal analysis, Data curation. **Yonghao Yuan:** Visualization, Investigation, Formal analysis. **Fang Han:** Project administration. **Kaifu Huo:** Supervision, Project administration, Funding acquisition. **Paul K. Chu:** . **Xuming Zhang:** Writing – review & editing, Resources, Conceptualization.

Declaration of competing interest

The authors declare that they have no known competing financial interests or personal relationships that could have appeared to influence the work reported in this paper.

Data availability

Data will be made available on request.

Acknowledgements

This work was financially supported by National Natural Science Foundation of China (Nos. 22379116, U2003130 and U2004210), Outstanding Youth Foundation of Natural Science Foundation of Hubei Province (2020CFA099), Innovation group of Key Research and Development Program of Hubei Province (2021BAA208 and 2022BCA061). City University of Hong Kong Donation Research Grant (DON-RMG no. 9229021). The authors are grateful to the facility support provided by the Analytical & Testing Center of Wuhan University of Science and Technology and Huazhong University of Science and Technology.

Appendix A. Supplementary data

Supplementary data to this article can be found online at https://doi.org/10.1016/j.microc.2024.111244.

References

[1] F. Martinon, Mechanisms of uric acid crystal-mediated autoinflammation, Immunol. Rev. 233 (2010) 218–232, https://doi.org/10.1111/j.0105-2896.2009.00860.x.
[2] M. Kuwabara, T. Fukuuchi, Y. Aoki, E. Mizuta, M. Ouchi, M. Kurajoh, et al., Exploring the multifaceted nexus of uric acid and health: A review of recent studies on diverse diseases, Biomolecules 13 (2023) 1519, https://doi.org/10.3390/biom13101519.
[3] K.L. Ong, L.K. Stafford, S.A. McLaughlin, E.J. Boyko, S.E. Vollset, A.E. Smith, et al, Global, regional, and national burden of diabetes from 1990 to 2021, with projections of prevalence to 2050: a systematic analysis for the Global Burden of Disease Study 2021, Lancet, 402(2023) 203-234. doi: 10.1016/S0140-6736(23)01301-6.
[4] M. Laakso, H. Cederberg, Glucose control in diabetes: which target level to aim for? J. Intern. Med. 272 (2012) 1–12, https://doi.org/10.1111/j.1365-2796.2012.02528.x.
[5] C.L. Benn, P. Dua, R. Gurrell, P. Loudon, A. Pike, R.I. Storer, et al., Physiology of hyperuricemia and urate-lowering treatments, Front. Med. 5 (2018), https://doi.org/10.3389/fmed.2018.00160.
[6] L.D. Ferguson, G. Molenberghs, G. Verbeke, K. Rahimi, S. Rao, I.B. McInnes, et al., Gout and incidence of 12 cardiovascular diseases: a case–control study including 152 663 individuals with gout and 709 981 matched controls, Lancet Rheumatol. 6 (2024) e156–e167, https://doi.org/10.1016/S2665-9913(23)00338-7.
[7] F. Li, X. Wang, J. Liu, Y. Hu, J. He, Double-layered microfluidic paper-based device with multiple colorimetric indicators for multiplexed detection of biomolecules, Sens Actuators B-Chem 288 (2019) 266–273, https://doi.org/10.1016/j.snb.2019.02.116.
[8] Y. Chen, Q. Zhong, Y. Wang, C. Yuan, X. Qin, Y. Xu, Colorimetric detection of hydrogen peroxide and glucose by exploiting the peroxidase-like activity of papain, RSC Adv. 9 (2019) 16566–16570, https://doi.org/10.1039/C9RA03111A.
[9] X. Wang, F. Li, Z. Cai, K. Liu, J. Li, B. Zhang, et al., Sensitive colorimetric assay for uric acid and glucose detection based on multilayer-modified paper with smartphone as signal readout, Anal. Bioanal. Chem. 410 (2018) 2647–2655, https://doi.org/10.1007/s00216-018-0939-4.
[10] Y. Liu, Y. Dong, M. Hui, L. Xu, L. Ye, J. Lv, et al., A biosensing array for multiplex clinical evaluation of glucose, creatinine, and uric acid, Biosens. Bioelectron. 241 (2023) 115699, https://doi.org/10.1016/j.bios.2023.115699.
[11] J. Zheng, M. Zhu, J. Kong, Z. Li, J. Jiang, Y. Xi, et al., Microfluidic paper-based analytical device by using Pt nanoparticles as highly active peroxidase mimic for simultaneous detection of glucose and uric acid with use of a smartphone, Talanta 237 (2022) 122954, https://doi.org/10.1016/j.talanta.2021.122954.
[12] W.-Y. Yang, J. Wang, X.-H. Li, B. Xu, Y.-W. Yang, L. Yu, et al., Analysis of non-targeted serum metabolomics in patients with chronic kidney disease and hyperuricemia, Biotechnol. Genet. Eng. Rev. (2023) 1–27, https://doi.org/10.1080/02648725.2023.2204715.
[13] M. Umer, M.U. Nisa, N. Ahmad, M.A. Rahim, L.M. Kasankala, Quantification of quercetin from red onion (Allium cepa L.) powder via High-Performance Liquid Chromatography-Ultraviolet (HPLC-UV) and its effect on hyperuricemia in male healthy Wistar albino rats, Food Sci Nutr, 12(2023) 1067-1081. doi: 10.1002/fsn3.3822.
[14] Z. Lv, B. Wang, B. Wang, H. Zhang, In vivo comprehensive metabolite profiling of esculetin and esculin derived from chicory in hyperuricemia rats using ultra-high-performance liquid chromatography coupled with quadrupole-orbitrap high-resolution mass spectrometry, J. Sep. Sci. 47 (1) (2023) 2300664, https://doi.org/10.1002/jssc.202300664.
[15] Y. Chen, Q. Yao, L. Zhang, P. Zeng, HPLC for simultaneous quantification of free mannose and glucose concentrations in serum: use in detection of ovarian cancer, Front. Chem. 11 (2023), https://doi.org/10.3389/fchem.2023.1289211.
[16] H. Xi, H. Gu, Y. Han, T. You, P. Wu, Q. Liu, et al., Peroxidase-like single Fe atoms anchored on $Ti_3C_2T_x$ MXene as surface enhanced Raman scattering substrate for the simultaneous discrimination of multiple antioxidants, Nano Res. 16 (2023) 10053–10060, https://doi.org/10.1007/s12274-023-5739-2.

[17] Q. Wang, D. Sun, X. Ma, R. Huang, J. Xu, X. Xu, et al., Surface enhanced Raman scattering active substrate based on hydrogel microspheres for pretreatment-free detection of glucose in biological samples, Talanta 260 (2023) 124657, https://doi.org/10.1016/j.talanta.2023.124657.
[18] F. Tian, L.F.d.C.e.S.d. Carvalho, A. Casey, M.S. Nogueira, H.J. Byrne, Surface-enhanced raman analysis of uric acid and hypoxanthine analysis in fractionated bodily fluids, Nanomater, 13(2023) 1216. doi: 10.3390/nano13071216.
[19] W. Peng, Z. Xu, X. Jia, Q. Liao, A copper foam-based surface-enhanced Raman scattering substrate for glucose detection, Discover Nano 18 (2023) 7, https://doi.org/10.1186/s11671-023-03776-x.
[20] D. Lu, R. Cai, Y. Liao, R. You, Y. Lu, Two-dimensional glass/p-ATP/Ag NPs as multifunctional SERS substrates for label-free quantification of uric acid in sweat, Spectrochim. Acta A Mol. Biomol. Spectrosc. 296 (2023) 122631, https://doi.org/10.1016/j.saa.2023.122631.
[21] S. Zhang, W. Zhao, C. Liu, J. Zeng, Z. He, C. Wang, et al., Flower-like CoO nanowire-decorated Ni foam: A non-invasive electrochemical biosensor for glucose detection in human saliva, Appl. Mater. Today 36 (2024) 102083, https://doi.org/10.1016/j.apmt.2024.102083.
[22] X. Ma, L. Deng, Z. Zou, Z. Pan, L. Feng, Z. Huang, et al., Novel portable photoelectrochemical sensor based on CdS/Au/TiO_2 nanotube arrays for sensitive, non-invasive, and instantaneous uric acid detection in saliva, Talanta 271 (2024) 125646, https://doi.org/10.1016/j.talanta.2024.125646.
[23] X. Xie, G. Mo, B. Hu, Electrochemical assembling of nano-MOFs at carbon fiber for the high-performance uric acid sensing, Sens Actuators B-Chem 393 (2023) 134263, https://doi.org/10.1016/j.snb.2023.134263.
[24] D. Jiang, T. Liu, Z. Chu, Y. Wang, Advances in nanostructured material-based non-enzymatic electrochemical glucose sensors, Anal, Methods 15 (2023) 6344–6361, https://doi.org/10.1039/D3AY01664A.
[25] S. Gengan, R.M. Gnanamuthu, S. Sankaranarayanan, V.M. Reddy, B.C. Marepally, R.K. Biroju, Electrochemical modified Pt nanoflower@rGO for non-enzymatic electrochemical sensing of glucose, Sens Actuators A-Phys 353 (2023) 114232, https://doi.org/10.1016/j.sna.2023.114232.
[26] J. Xu, N. Xu, X. Zhang, P. Xu, B. Gao, X. Peng, et al., Phase separation induced rhizobia-like Ni nanoparticles and TiO_2 nanowires composite arrays for enzyme-free glucose sensor, Sens Actuators B-Chem 244 (2017) 38–46, https://doi.org/10.1016/j.snb.2016.12.088.
[27] J. Xu, N. Xu, X. Zhang, B. Gao, B. Zhang, X. Peng, et al., In situ fabrication of Ni nanoparticles on N-doped TiO_2 nanowire arrays by nitridation of $NiTiO_3$ for highly sensitive and enzyme-free glucose sensing, J. Mater. Chem. B 5 (2017) 1779–1786, https://doi.org/10.1039/C6TB02784A.
[28] K. Huo, Y. Li, R. Chen, B. Gao, C. Peng, W. Zhang, et al., Recyclable Non-Enzymatic Glucose Sensor Based on Ni/$NiTiO_3$/TiO_2 Nanotube Arrays, ChemPlusChem 80 (2015) 576–582, https://doi.org/10.1002/cplu.201402288.
[29] F. Zhou, C. You, Q. Wang, Y. Chen, Z. Wang, Z. Zeng, et al., 3D shell-core structured NiCu-OH@Cu$(OH)_2$ nanorod: A high-performance catalytic electrode for non-enzymatic glucose detection, J. Electroanal. Chem. 876 (2020) 114477, https://doi.org/10.1016/j.jelechem.2020.114477.
[30] P. Wu, J. Fan, Y. Tai, X. He, D. Zheng, Y. Yao, et al., Ag@TiO_2 nanoribbon array: a high-performance sensor for electrochemical non-enzymatic glucose detection in beverage sample, Food Chem. 447 (2024) 139018, https://doi.org/10.1016/j.foodchem.2024.139018.
[31] M. Wei, Y. Qiao, H. Zhao, J. Liang, T. Li, Y. Luo, et al., Electrochemical non-enzymatic glucose sensors: recent progress and perspectives, Chem. Commun. 56 (2020) 14553–14569, https://doi.org/10.1039/D0CC05650B.
[32] C. Hang, Y. Qin, G. Tian, J. Hu, W. Li, J. Wu, New insight into the mechanism of simultaneous determination of ascorbic acid, dopamine, and uric acid with graphene encapsulated CoFe alloys electrochemical sensor, Adv. Mater. Interfaces 9 (2022) 2200774, https://doi.org/10.1002/admi.202200774.
[33] A. Gao, X. Zhang, X. Peng, H. Wu, L. Bai, W. Jin, et al., In situ synthesis of Ni$(OH)_2$/TiO_2 composite film on NiTi alloy for non-enzymatic glucose sensing, Sens Actuators B-Chem 232 (2016) 150–157, https://doi.org/10.1016/j.snb.2016.03.122.
[34] L. Hu, K. Huo, R. Chen, X. Zhang, J. Fu, P.K. Chu, Core-shell TiC/C quasi-aligned nanofiber arrays on biomedical Ti6Al4V for sensitive electrochemical biosensing, Chem. Commun. 46 (2010) 6828–6830, https://doi.org/10.1039/C0CC00804D.
[35] X. Zhang, L. Li, X. Peng, R. Chen, K. Huo, P.K. Chu, Non-enzymatic hydrogen peroxide photoelectrochemical sensor based on WO_3 decorated core-shell TiC/C nanofibers electrode, Electrochim. Acta 108 (2013) 491–496, https://doi.org/10.1016/j.electacta.2013.07.064.
[36] X. Zhang, K. Huo, X. Peng, R. Xu, P. Li, R. Chen, et al., WO_3 nanoparticles decorated core-shell TiC-C nanofiber arrays for high sensitive and non-enzymatic photoelectrochemical biosensing, Chem. Commun. 49 (2013) 7091–7093, https://doi.org/10.1039/C3CC42583E.
[37] I. Anshori, L.R. Ula, G.I.N. Asih, E. Ariasena, Uperianti, A.N. Raditya, et al., Durable nonenzymatic electrochemical sensing using silver decorated multi-walled carbon nanotubes for uric acid detection, Nanotechnology, 35(2023) 115501. doi: 10.1088/1361-6528/ad143f.
[38] L. Zhang, L. Yu, J. Peng, X. Hou, H. Du, Highly sensitive and simultaneous detection of ascorbic acid, dopamine, and uric acid using Pt@g-C_3N_4/N-CNTs nanocomposites, iScience, 27(2024) 109241. doi: 10.1016/j.isci.2024.109241.
[39] F. Wang, F. Shi, J. Li, N. Chen, C. Chen, Z. Xu, et al., Cu microspheres decorated ZnO@CNT/Carbon cloth flexible biosensor for simultaneous determination of glucose and uric acid, Microchem. J. 193 (2023) 109054, https://doi.org/10.1016/j.microc.2023.109054.
[40] R. Li, H. Liang, M. Zhu, M. Lai, S. Wang, H. Zhang, et al., Electrochemical dual signal sensing platform for the simultaneous determination of dopamine, uric acid and glucose based on copper and cerium bimetallic carbon nanocomposites, Bioelectrochemistry 139 (2021) 107745, https://doi.org/10.1016/j.bioelechem.2021.107745.
[41] Y. Wen, M.D.R. Kok, J.P.V. Tafoya, A.B.J. Sobrido, E. Bell, J.T. Gostick, et al., Electrospinning as a route to advanced carbon fibre materials for selected low-temperature electrochemical devices: A review, J Energy Chem 59 (2021) 492–529, https://doi.org/10.1016/j.jechem.2020.11.014.
[42] Y. Liu, J. Luo, C. Helleu, M. Behr, H. Ba, T. Romero, et al., Hierarchical porous carbon fibers/carbon nanofibers monolith from electrospinning/CVD processes as a high effective surface area support platform, J. Mater. Chem. A 5 (2017) 2151–2162, https://doi.org/10.1039/C6TA09414G.
[43] C.P. Deck, K. Vecchio, Growth mechanism of vapor phase CVD-grown multi-walled carbon nanotubes, Carbon 43 (2005) 2608–2617, https://doi.org/10.1016/j.carbon.2005.05.012.
[44] B. McLean, I. Mitchell, F. Ding, Mechanism of alcohol chemical vapor deposition growth of carbon nanotubes: catalyst oxidation, Carbon 191 (2022) 1–9, https://doi.org/10.1016/j.carbon.2022.01.046.
[45] H. Yin, X. Bai, Z. Yang, Activating Ni nanoparticles into Ni single atoms by N doping for high-performance electrochemical sensing of glucose, Chem. Eng. J. 478 (2023) 147510, https://doi.org/10.1016/j.cej.2023.147510.
[46] A. Stanoiu, C. Ghica, C.G. Mihalcea, D. Ghica, S. Somacescu, O.G. Florea, et al., effects of calcination temperature on CO-sensing mechanism for NiO-based gas sensors, Chemosensors 10 (2022) 191, https://doi.org/10.3390/chemosensors10050191.
[47] J. Gao, Y. Wang, H. Wu, X. Liu, L. Wang, Q. Yu, et al., Construction of a sp^3/sp^2 carbon interface in 3D N-doped nanocarbons for the oxygen reduction reaction, Angew. Chem. Int. Ed. 58 (2019) 15089–15097, https://doi.org/10.1002/anie.201907915.
[48] C. Pi, C. Huang, Y. Yang, H. Song, X. Zhang, Y. Zheng, et al., In situ formation of N-doped carbon-coated porous MoP nanowires: a highly efficient electrocatalyst for hydrogen evolution reaction in a wide pH range, Appl Catal B-Environ 263 (2020) 118358, https://doi.org/10.1016/j.apcatb.2019.118358.
[49] M. Marciuš, M. Ristić, M. Ivanda, S. Musić, Formation and microstructure of nickel oxide films, J Alloys Compounds 541 (2012) 238–243, https://doi.org/10.1016/j.jallcom.2012.07.021.
[50] Z. Li, L. Deng, I.A. Kinloch, R.J. Young, Raman spectroscopy of carbon materials and their composites: graphene, nanotubes and fibres, Prog. Mater Sci. 135 (2023) 101089, https://doi.org/10.1016/j.pmatsci.2023.101089.
[51] F. Vasiliou, A.K. Plessas, A. Economou, N. Thomaidis, G.S. Papaefstathiou, C. Kokkinos, Graphite paste sensor modified with a Cu(II)-complex for the enzyme-free simultaneous voltammetric determination of glucose and uric acid in sweat, J. Electroanal. Chem. 917 (2022) 116393, https://doi.org/10.1016/j.jelechem.2022.116393.
[52] C. Xiong, T. Zhang, W. Kong, Z. Zhang, H. Qu, W. Chen, et al., ZIF-67 derived porous Co_3O_4 hollow nanopolyhedron functionalized solution-gated graphene transistors for simultaneous detection of glucose and uric acid in tears, Biosens. Bioelectron. 101 (2018) 21–28, https://doi.org/10.1016/j.bios.2017.10.004.
[53] J. Gao, W. Huang, Z. Chen, C. Yi, L. Jiang, Simultaneous detection of glucose, uric acid and cholesterol using flexible microneedle electrode array-based biosensor and multi-channel portable electrochemical analyzer, Sens Actuators B-Chem 287 (2019) 102–110, https://doi.org/10.1016/j.snb.2019.02.020.
[54] M. Faruk Hossain, G. Slaughter, Flexible electrochemical uric acid and glucose biosensor, Bioelectrochemistry, 141(2021) 107870. doi: 10.1016/j.bioelechem.2021.107870.

Supplementary Material

Potential-Dependent Simultaneous Detection of Uric Acid and Glucose Using Dual-Function Ni@CNT Supported Carbon Fiber Electrodes

Biyuan Zhou [a], Jijiang Fu [a],Yonghao Yuan [a], Fang Han [b*], Kaifu Huo [c], Paul K. Chu [d], Xuming Zhang [a*]

[a] The State Key Laboratory of Refractories and Metallurgy and Institute of Advanced Materials and Nanotechnology, Wuhan University of Science and Technology, Wuhan 430081, China

[b] School of Chemistry and Chemical Engineering, Wuhan University of Science and Technology, ,Wuhan 430081, China

[c] Wuhan National Laboratory for Optoelectronics (WNLO) School of Optical and Electronic Information, Huazhong University of Science and Technology, Wuhan 430074, China

[d] Department of Physics, Department of Materials Science and Engineering, and Department of Biomedical Engineering, City University of Hong Kong, Tat Chee Avenue,Kowloon, Hong Kong, China

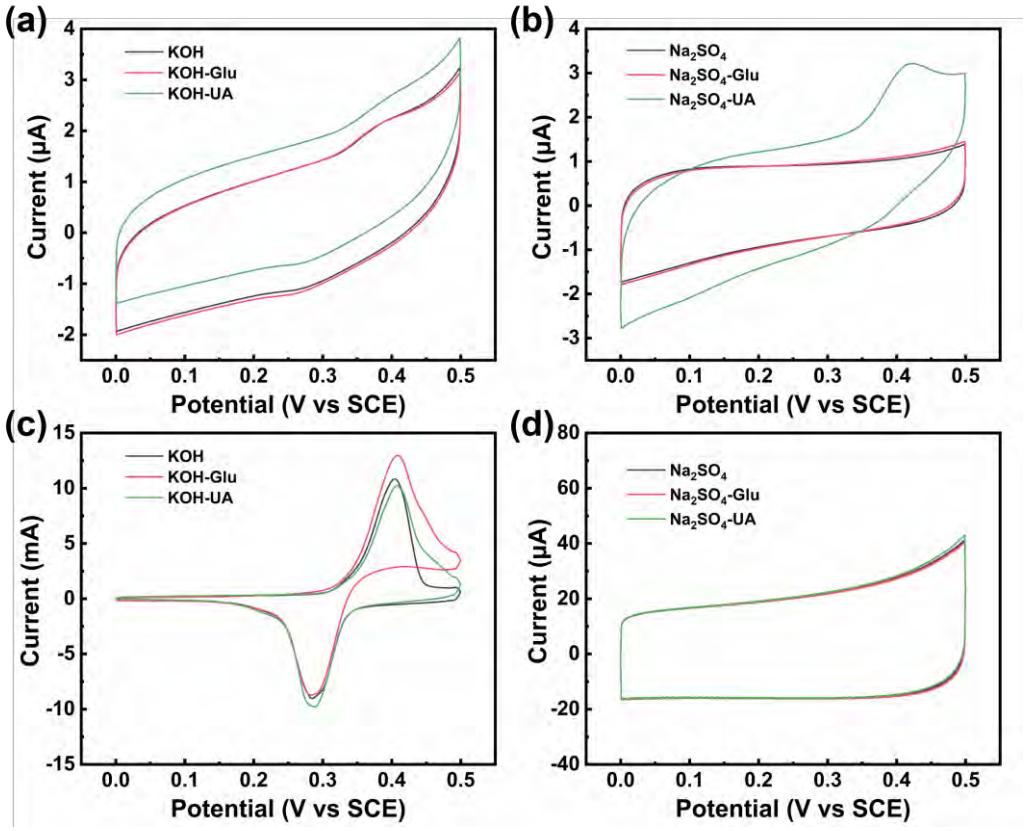

Figure S1 (a) and (c) CV curves of GCE and metal Ni foil at a sweep rate of 100 mV/s before and after adding UA and glucose in 1 M KOH solution, respectively; (b) and (d) CV curves of GCE and metal Ni foil at a sweep rate of 100 mV/s before and after adding UA and glucose in 0.1 M Na_2SO_4 solution respectively.

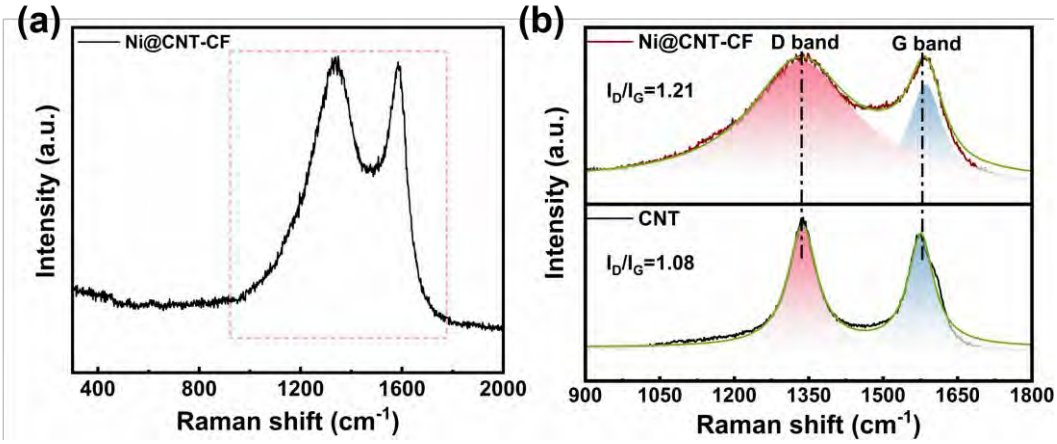

Figure S2 (a) Raman spectra of Ni@CNT-CF; (b) Comparison between Raman spectra of Ni@CNT-CF and CNT in the range of 900 to 1800 cm^{-1}.

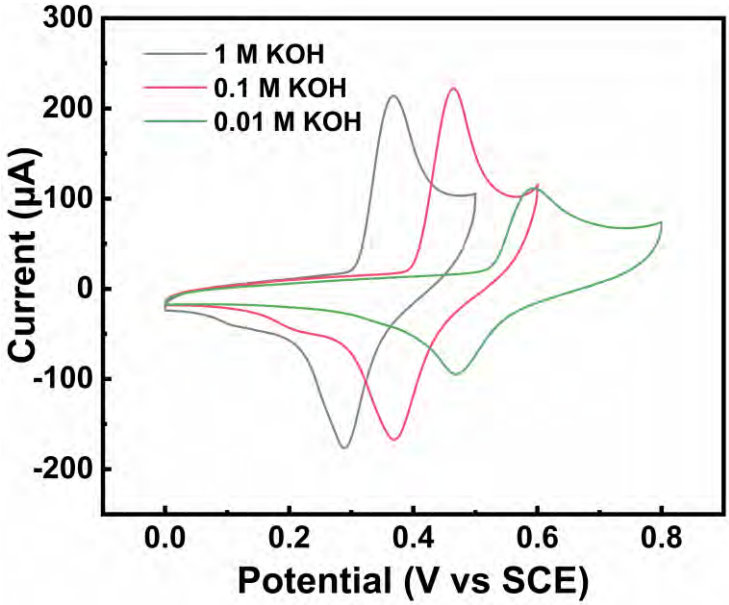

Figure S3 CV curves of Ni@CNT-CF in different concentrations of KOH solutions at a sweep rate of 100 mV/s.

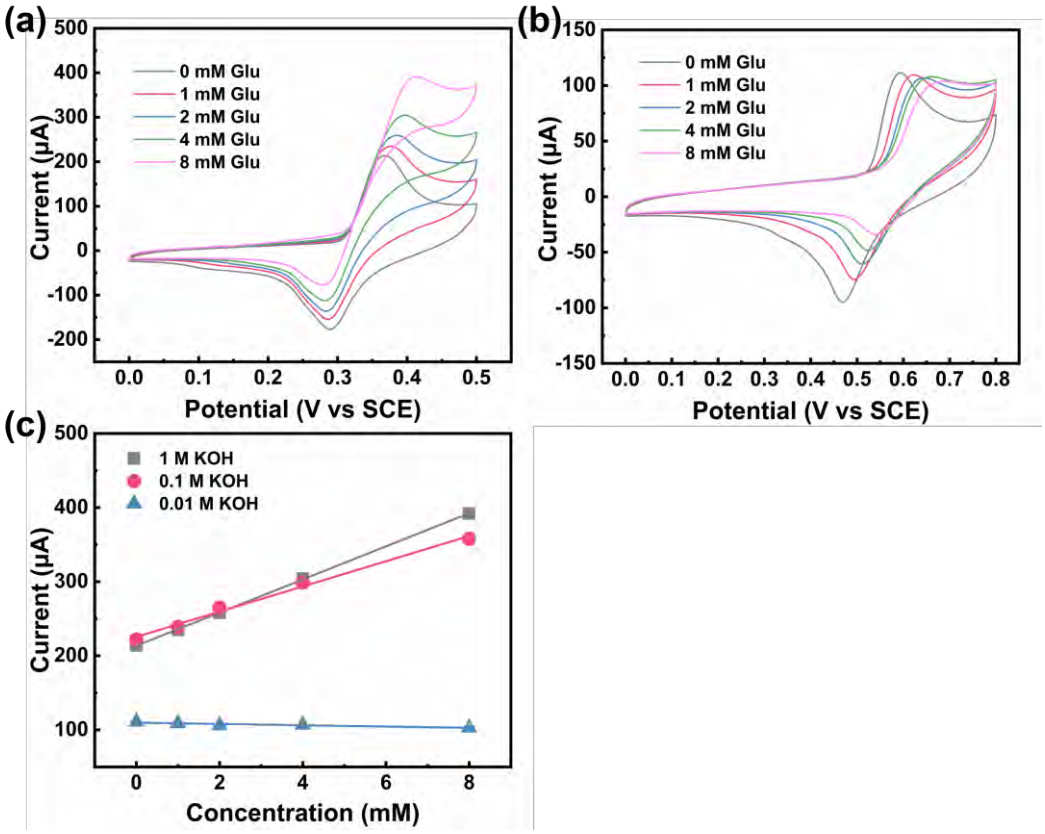

Figure S4 CV curves of Ni@CNT-CF with different amounts of glucose at a sweep rate of 100 mV/s in (a) 1 M KOH and (b) 0.01 M KOH solution; (c) Corresponding fitted line based on the oxidized peak current to glucose concentration.

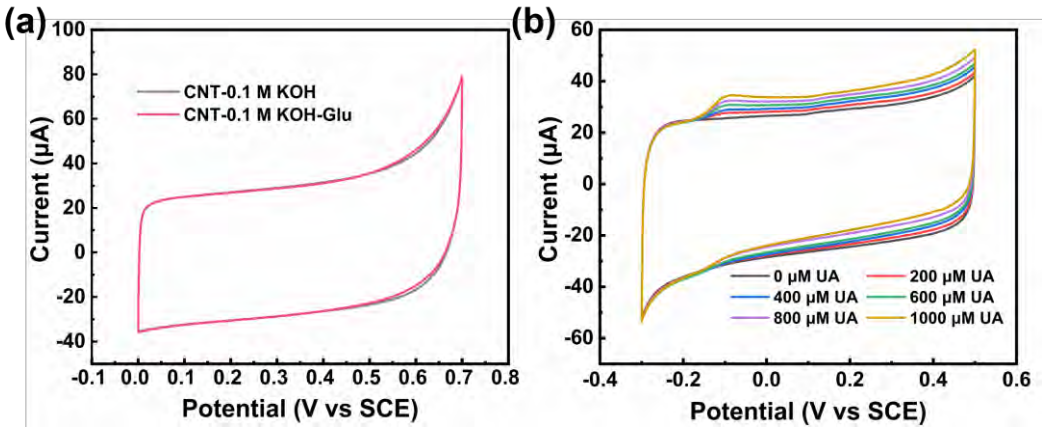

Figure S5 (a) CV curves of CNT electrode before and after adding glucose in 0.1 M KOH solution at a sweep rate of 100 mV/s; (b) CV curves of CNT electrode after adding different amounts of UA in 0.1 M KOH solution at a sweep rate of 100 mV/s.

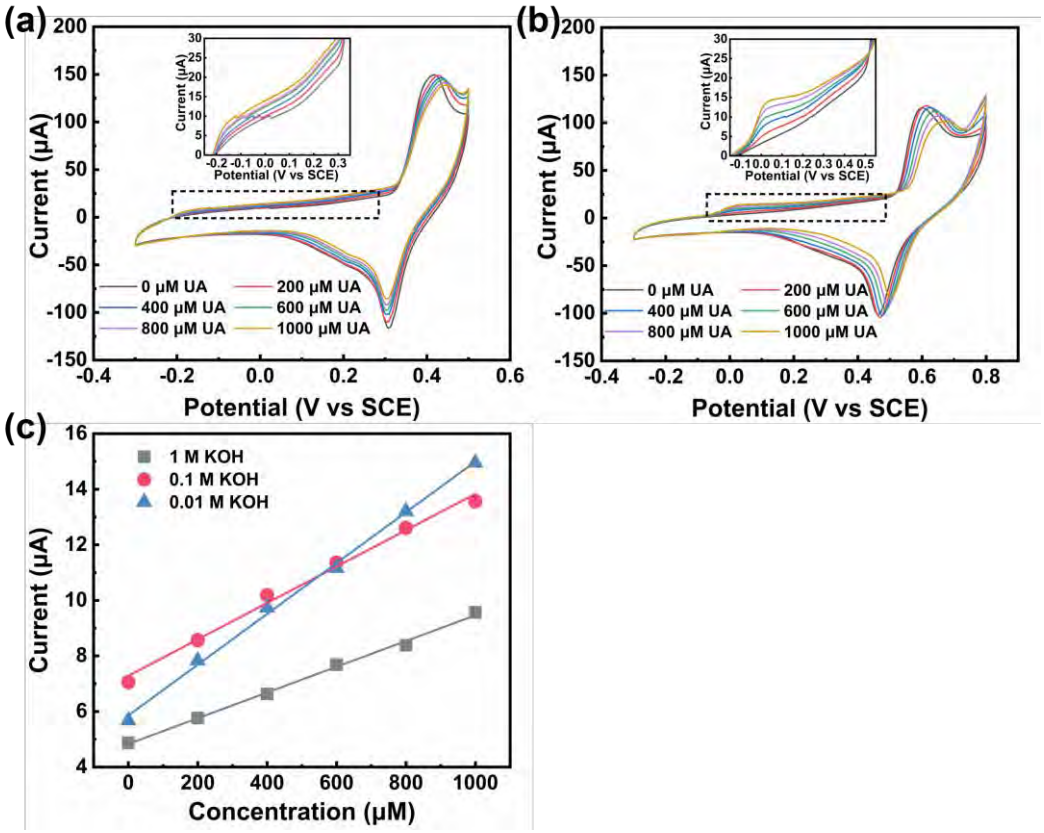

Figure S6 CV curves of Ni@CNT-CF with different amounts of UA at a sweep rate of 100 mV/s in (a) 1 M KOH and (b) 0.01 M KOH solution; (c) Corresponding fitted line based on the oxidized peak current to UA concentration.

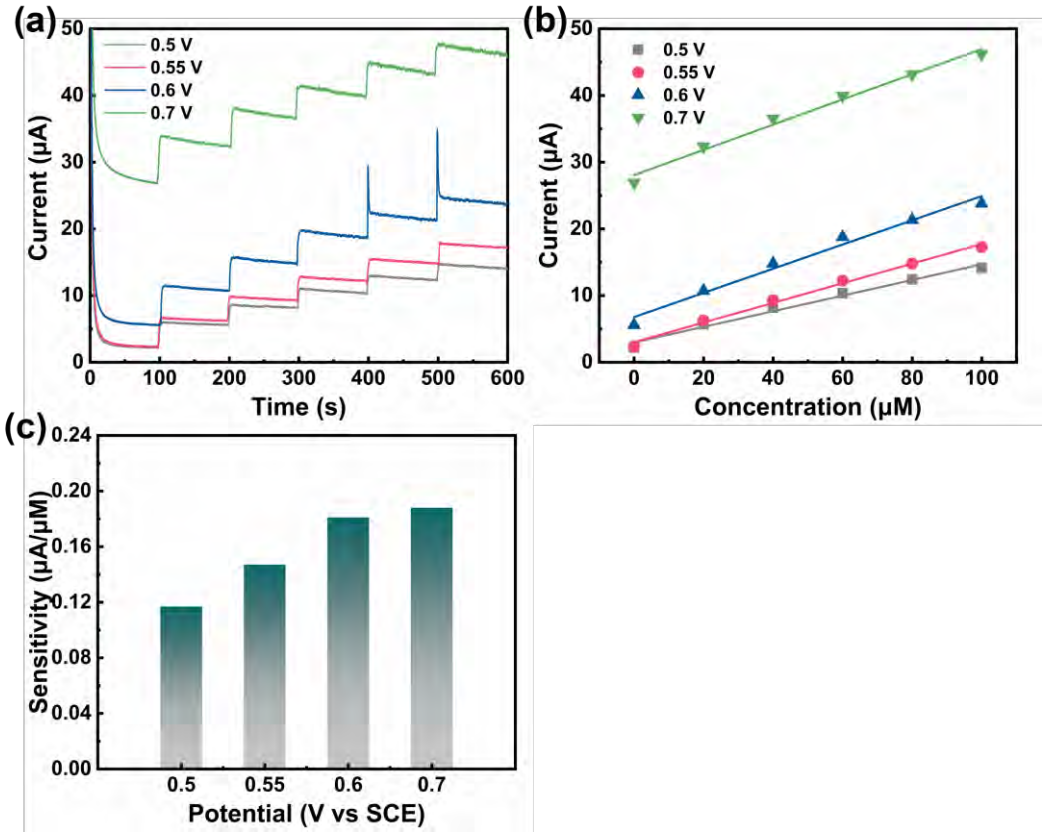

Figure S7 (a) I-t response of Ni@CNT-CF by sequentially adding 200 μM glucose at potentials ranging from 0.5 V to 0.7 V; (b) corresponding fitted plot between UA concentration and current increment; (c) corresponding sensitivity at different potentials.

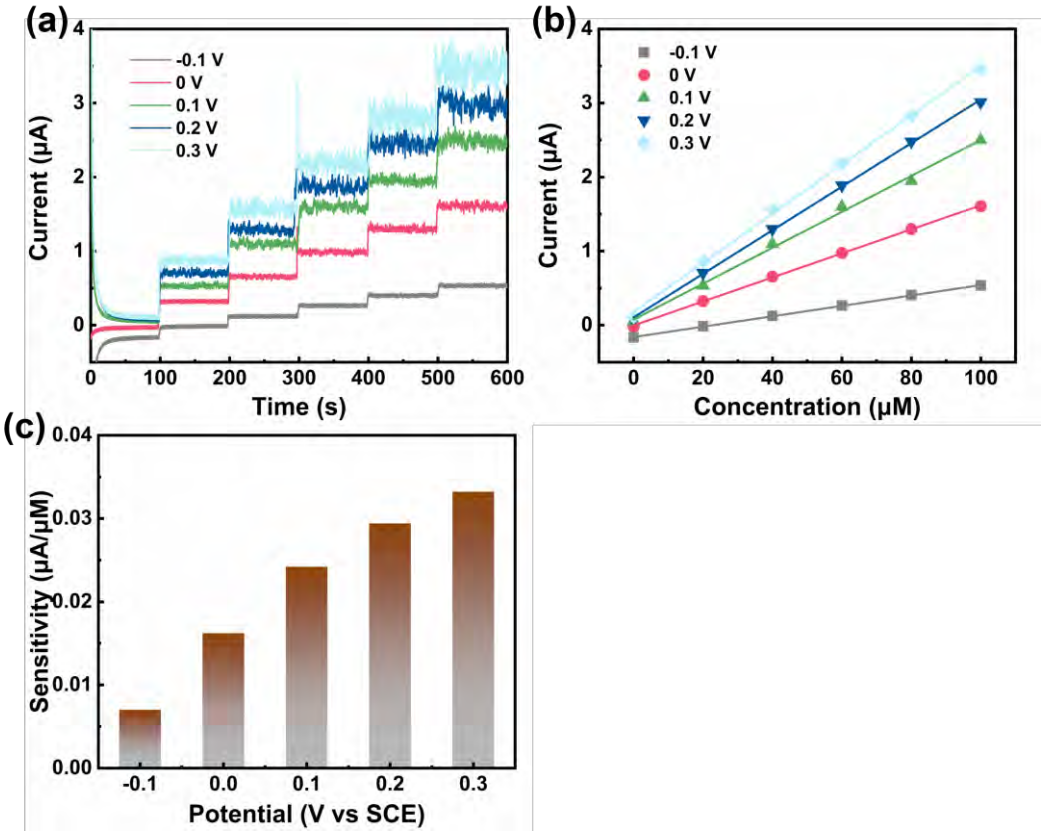

Figure S8 (a) I-t response of Ni@CNT-CF by sequentially adding 200 μM UA at potentials ranging from -0.1 V to 0.3 V; (b) corresponding fitted plot between UA concentration and current increment; (c) corresponding sensitivity at different potentials.

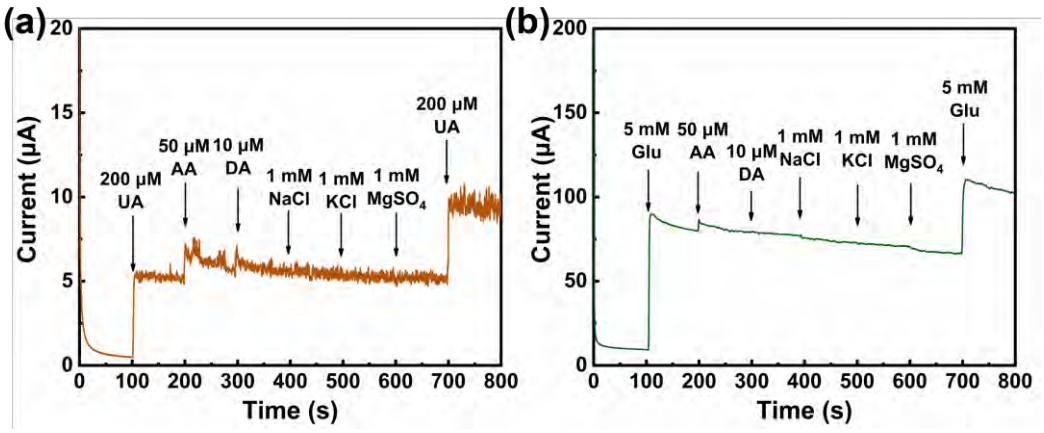

Figure S9 (a) Selectivity test of Ni@CNT-CF at 0.2 V by adding 50 μM AA, 10 μM DA, 1 mM potassium chloride, 1 mM sodium chloride, and 1 mM magnesium sulfate to 0.1 M KOH containing 200 μM UA; (b) Selectivity test of Ni@CNT-CF at 0.6 V by adding 50 μM AA, 10 μM DA, 1 mM potassium chloride, 1 mM sodium chloride, and 1 mM magnesium sulfate to 0.1 M KOH containing 5 mM glucose.

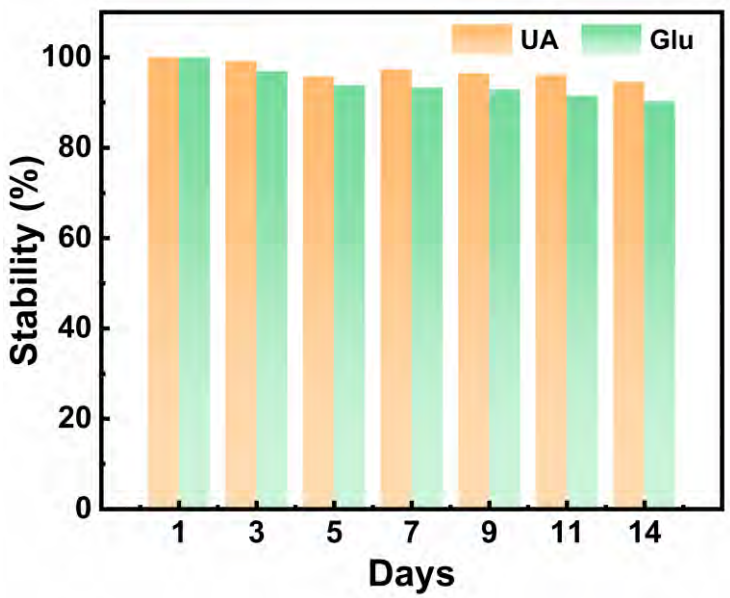

Figure S10 Stability of Ni@CNT-CF electrode for UA and glucose detection within 14 days.

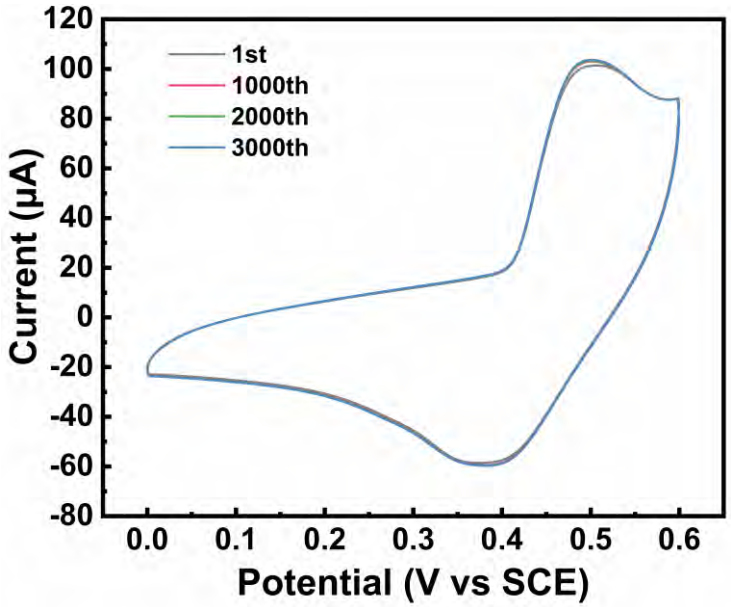

Figure S11 CV curves of the Ni@CNT-CF electrode cycled 3000 times at a sweep rate of 100 mV/s in 0.1 M KOH solution.

Table S1 Potential difference between glucose and UA on Ni@CNT-CF electrode at different KOH concentrations.

Test substance	Oxidation potential		
	1 M KOH	**0.1 M KOH**	**0.01 M KOH**
1 mM Glu	0.37 V	0.46 V	0.62 V
200 μM UA	0.01 V	0.03 V	0.04 V
ΔE (E_{Glu}-E_{UA})	0.36 V	0.43 V	0.58 V

According to Nernst equation ($E = E_0 - (RT)/(nF)*\ln(1/[OH^-])$), for glucose oxidation, reaction 1 is the electrochemical control step, reaction 2 is the self-oxidation reaction, so, the n is 1.

$$NiO + OH^- \Leftrightarrow NiOOH + e^- \quad (1)$$

$$Ni^{3+} + \text{glucose} \rightarrow Ni^{2+} + \text{gluconic acid} \quad (2)$$

$$UA + 2OH^- \rightarrow UA_{ox} + 2H_2O + 2e^- \quad (3)$$

For UA oxidation (UA_{ox}), two electrons and two protons are removed from UA, where n is 2. Consequently, the slope value of RT/nF for the UA oxidation reaction is half that of the glucose oxidation reaction. Therefore, the potential difference between glucose and UA increases as the concentration of KOH decreases.

Table S2 The fitting test parameter values based on different linear regression models.

Substance	Concentration range (μM)	Pearson's correlation coefficient (R)	R^2	Lack of fit test	
				F value	$F_{crit,95\%}$
UA	1-20	0.991	0.978	0.503	1.966
	20-1000	0.997	0.995	0.049	2.043
Glu	1-100	0.998	0.996	0.049	1.966
	100-6000	0.991	0.977	0.061	2.139

The formulas for the lack-of-fit (LoF) method are listed as follows:

$$F = \frac{MSS_{LoF}}{MSS_e} = \frac{\sum(\bar{y}_i - \hat{y}_i)^2/n-2}{\sum(y_i - \bar{y}_i)^2}/n(p-1)$$

Where the MSS_{LoF} represents the mean sum of squares (with n-2 degrees of freedom) and MSSe represents the mean sum of squares of the random error (with n(p-1) degrees of freedom), n represents the total number of observations, and p represents the number of unique values. By calculation, the observed F values are all lower than the critical F values in the 95% confidence interval, indicating that the linear model data are reliable.

Table S3 The electrochemical sensing performance of Ni@CNT-CF electrode for glucose and UA in comparison with thses previously reported non-enzymatic biosensors.

Modified electrode	Analytes	Linear range	LOD	Ref
GR-SWCNT-Ce-Cu	UA	0.08-100 μM	6.3 nM	Bioelectrochemistry, 139(2021) 107745.
	Glucose	1-40; 40-1000 μM	95 nM	
Cu(II)-Complex	UA	50-500 μM	4.6 μM	J Electroanal Chem, 917(2022) 116393.
	Glucose	20-400 μM	5 μM	
CHIT/Co_3O_4/Au	UA	0.3-3 μM	0.1 μM	Biosens Bioelectron, 101(2018) 21-28.
	Glucose	0.01-0.3 mM	0.1 μM	
Pt NPs/PANI/MEA	UA	0.1-1.2 mM	4 μM	Sens Actuators B-Chem, 287(2019) 102-110.
	Glucose	2-12 mM	260 μM	
LSG/PBSE/PtNPs	UA	5-480 μM	0.18 μM	Bioelectrochemistry, 141(2021) 107870.
	Glucose	2.5-2500 μM	2.35 μM	
Pt-NPs-μPADs	UA	0.01-2.5 mM	3 μM	Talanta, 237(2022) 122954.
	Glucose	0.01-5 mM	4 μM	
Cu MSs/ZnO@CNTs/CC	UA	5-240 μM	0.18 μM	Microchem J, 193(2023) 109054.
	Glucose	2.5-1000 μM	0.11 μM	
Ni@CNT-CF	**UA**	**1-1000 μM**	**0.32 μM**	**Our work**
	Glucose	**1-6000 μM**	**0.39 μM**	

Table S4 The recovery of Ni@CNT-CF electrode for the determination of UA and glucose (Glu) in simulated fluid and human serum.

Sample		Standard value (C)	Electrochemical testing (C_1)	Average Recovery (%)	UA/Glu meter testing (C_2)	Recovery ($\frac{C_2}{C}$×100%)
Simulated fluid	UA	400 μM	423.8 μM	98.2 ±5.7%	435 μM	108.7%
	UA	400 μM	388.5 μM			
	UA	400 μM	367.7 μM			
	Glu	5 mM	5.78 mM	108.9 ±4.7%	4.2 mM	84%
	Glu	5 mM	5.31 mM			
	Glu	5 mM	5.26 mM			
Human serum	UA	260 μM	272.3 μM	104.7%	285 μM	109.6%
	Glu	6.6 mM	6.9 mM	104.5%	7.1 mM	107.3%